Published in final edited form as:
Nat Neurosci. 2020 April ; 23(4): 565–574. doi:10.1038/s41593-020-0593-y.

Specialized medial prefrontal-amygdala coordination in other-regarding decision preference

Olga Dal Monte[1,2], **Cheng C. J. Chu**[1], **Nicholas A. Fagan**[1], **Steve W. C. Chang**[1,3,4,*]

[1]Department of Psychology, Yale University, New Haven, CT 06520

[2]Department of Psychology, University of Turin, Torino, Italy

[3]Department of Neuroscience, Yale University School of Medicine, New Haven, CT 06510

[4]Kavli Institute for Neuroscience, Yale University School of Medicine, New Haven, CT 06510

Abstract

Social behaviors recruit multiple cognitive operations that require interactions between cortical and subcortical brain regions. Interareal synchrony may facilitate such interactions between cortical and subcortical neural populations. However, it remains unknown how neurons from different nodes in the social brain network interact during social decision-making. Here, we investigated oscillatory neuronal interactions between the basolateral amygdala and the rostral anterior cingulate gyrus of the medial prefrontal cortex while monkeys expressed context-dependent positive or negative other-regarding preference (ORP), where decisions impacted the reward received by another monkey. Synchronization between the two nodes was enhanced for positive ORP, but suppressed for negative ORP. These interactions occurred in beta and gamma frequency bands depending on the area contributing spikes, exhibited a specific directionality of information flow associated with positive ORP, and could be used to decode social decisions. These findings suggest that specialized coordination in the medial prefrontal-amygdala network underlies social-decision preference.

Keywords

anterior cingulate cortex; amygdala; medial prefrontal cortex; coherence; spikes; local field potential; social decision-making

Altruistic behaviors and mutually beneficial social exchanges facilitate cohesion among members of a group and help attain collective rewards. While selfish behaviors can be detrimental to these causes, they may be strategically necessary to secure limited resources

---

[*]Corresponding Author: Steve W. C. Chang, Ph.D., steve.chang@yale.edu, Tel: 1-314-307-0498.

Author Contributions
S.W.C.C. and O.D.M. designed the study and wrote the paper. O.D.M. performed the experiments. C.J.C., N.A.F., O.D.M., and S.W.C.C. analyzed the data.

Competing Financial Interests
The authors declare no competing financial interests.

or achieve a certain social status. The cognitive operations central to making such social decisions are theorized to recruit multiple brain regions that are sensitive to primary and more abstract rewards, and span cortical and subcortical areas with divergent functional specifications[1–5].

Single-neuron studies using social interaction paradigms have begun to characterize neuronal correlates of social decision variables concerning conspecific animals in several brain regions. These regions include the anterior cingulate cortex (ACC)[6,7], dorsomedial prefrontal cortex[8], basolateral amygdala (BLA)[9–11], orbitofrontal cortex (OFC)[6,12], striatum[13], and lateral prefrontal cortex[14,15]. Of these, the gyrus of the rostral ACC (ACCg) of the medial prefrontal cortex is thought to be particularly specialized in signaling rewarding and motivational information about social partners in humans and monkeys[1,16]. When monkeys express other-regarding preferences (ORP) by choosing to deliver juice rewards to a conspecific monkey over discarding the rewards, some ACCg cells exclusively encode conspecific's rewards while other cells encode one's own and conspecific's rewards in an indistinguishable manner[6]. By contrast, OFC or ACC sulcus neurons in this paradigm predominantly signal self-referenced decision variables by modulating firing rates only in relation to one's received or foregone rewards[6]. These findings lend support for the role of rostral ACCg in computing other-referenced variables[16]. Conversely, BLA neurons exhibit correlated value-tuned activity for encoding choices that result in juice rewards to either themselves or a conspecific monkey[9], suggesting that BLA utilize a shared metric for decision variables between self and other. Similar characteristics have later been observed in ACCg and BLA neurons in the human brain from an intracranial study[17].

Coherence between specific nodes in the social brain network likely plays a key role in social behavior. Human functional neuroimaging studies have implicated the importance of correlated activations involving different brain regions in social cognition[18,19]. In prairie voles, frequency-specific coupling between medial prefrontal cortex and nucleus accumbens mediates social bonding[20]. Moreover, BLA-projecting ACC neurons are necessary for observational fear learning in mice[21]. In turn, dysregulated subcortical-medial prefrontal synchrony could result in abnormal social behaviors[22]. However, neuronal mechanisms underlying interareal synchrony associated with complex social behaviors in primates, such as those related to positive or negative ORP, remain elusive.

Reciprocal and dense projections between ACCg and BLA permit the two nodes to efficiently communicate social and affective information[23,24]. However, whether and how ACCg and BLA coordinate activity for social decision-making remain unknown. If coordinated interactions between ACCg and BLA were involved in the expression of either positive or negative ORP concerning the welfare of others, one might expect distinctive coordination patterns to exist for two different types of ORPs. Such interaction may be mediated by a dedicated frequency channel with a specific information flow between ACCg and BLA associated with expressing a particular ORP. To test this, we investigated how single-neuron spiking and local field potential (LFP) activity between ACCg and BLA are dynamically coordinated as monkeys expressed positive or negative ORP toward a conspecific monkey. We used spike-field coherence as our primary measure as it quantifies how spikes from one region is synchronized to oscillatory LFP signals from another region in discrete time and frequency windows, allowing inspections of synchronous coordination of neural activity between brain areas[25,26].

We found that synchrony between spikes and LFP oscillations between the two nodes differentiated monkeys' positive ORP in one context from negative ORP in another context. Moreover, these synchrony patterns were specific to select frequency bands and time windows, and support a directional transfer of information between the two nodes. Unique rhythmic coordination of neuronal activity in the primate medial prefrontal-amygdala network may thus contribute to social decision-making.

Results

Monkeys exhibit positive and negative ORPs in distinct contexts

Pairs of rhesus macaques (an actor and a recipient) participated in the social reward allocation task (Fig. 1a–b; Online Methods). In one decision context (*Other*/*Bottle* context) where actor monkeys never received juice rewards, actors were free to choose between donating a juice drop to a recipient (*Other*) and to a juice collection bottle (*Bottle*). In the other decision context (*Self*/*Both* context) where actors always received juice rewards, actors were free to choose between delivering rewards to themselves (*Self*) and to both themselves and the other monkey (*Both*). This task therefore measures actor's social decision preference without self-reward confound in choosing one option over the other in two separate contexts.

Actors completed 313 ± 109 (mean ± s.d.) trials per session over 57 sessions (monkey H: 374 ± 110 per session, 31 sessions; monkey K: 240 ± 43 per session, 26 sessions). Consistent with previous findings using this design[6,9,27,28], actors preferred to choose *Other* over *Bottle*, exhibiting a positive ORP (preference index, mean ± s.e.m.: 0.32 ± 0.02, $p < 0.0001$, Wilcoxon sign rank) in the *Other*/*Bottle* context, but preferred to choose *Self* over *Both*, displaying a negative ORP in the *Self*/*Both* context (–0.08 ± 0.02, $p < 0.001$) (Fig. 1c). These context-dependent preferences were consistent over time of each session (*Self*/*Both* and *Other*/*Bottle* context: both $p > 0.52$, linear regression, Fig. 1c)[9,27], have been observed in several different animals in independent studies[6,9,27,28], are sensitive to pair dominance and familiarity[27], and are abolished if the recipient monkey is replaced with a juice collection bottle[27].

Social gaze patterns differed as a function of decision (*Self*, *Both*, *Other*, *Bottle*) ($F[3, 455] = 2.86$, $p = 0.037$) and gaze-goal (recipient or bottle) ($F[1, 455] = 10.66$, $p = 0.001$). Critically, decision type and gaze-goal showed a strong interaction ($F[3, 455] = 8.75$, $p < 0.0001$), indicating that social gaze differed for decision types. Actors overall looked at the recipient (36 ± 1% [mean ± s.e.m.]) at a higher rate than to the bottle (30 ± 1%, $p = 0.001$, Tukey test). Importantly, after choosing *Other,* actors looked at the recipient (41 ± 2%) more frequently compared to the bottle (26 ± 2%, $p < 0.0001$). By contrast, actors looked at the bottle more often after choosing *Bottle* (37 ± 3%) than after choosing *Other* (26 ± 2%) ($p = 0.002$) (Fig. 1d). These observations support that actors were acutely aware of the reward outcomes between the conditions in which rewards were either allocated to the recipient or the bottle, the two outcomes without a self-reward contingency[6,9,27,28]. These context-dependent social decision preferences provide a behavioral framework for examining the coordination between ACCg and BLA in expressing positive and negative ORPs toward a conspecific monkey under different contexts.

On free-choice trials, actors overall completed more *Self/Both* trials (greater than 99% for all reward sizes) compared to *Other/Bottle* trials (87% for all reward sizes) (F[1,341] = 175.12, $p < 0.0001$) (Fig. 1e). However, actors were more motivated to complete *Other/Bottle* trials when the reward size at stake for either the recipient or the bottle was larger (small: 83 ± 2%, medium: 87 ± 2%, large: 90 ± 2%; F[2,168] = 4.3, p = 0.02). On forced-choice trials, performance was at ceiling and did not differ between outcomes. Saccade reaction times on free-choice trials differed as a function of decision (*Self* [197 ms ± 27 ms], *Both* [200 ms ± 29 ms], *Other* [278 ms ± 43 ms], *Bottle* [271 ms ± 59 ms]; F[3, 215] = 59, $p < 0.0001$) (Fig. 1f), driven by the differences in reaction times for receiving rewards (*Self* or *Both*) compared to forgoing rewards (*Other* or *Bottle*) ($p < 0.0001$, Wilcoxon rank sum; *Self* vs. *Both* [p = 0.96], *Other* vs. *Bottle* [p = 0.75]; *Self* or *Both* vs. *Other* or *Bottle*, all $p < 0.001$, Tukey test).

Coordination of spiking and LFP activity between ACCg and BLA

Exploiting context-dependent positive and negative ORPs, we investigated neural coordination for the two types of ORPs between rostral ACCg (Brodmann areas 24a, 24b, and 32)[29] and BLA[29] (Fig. 2). All single units were recorded without any sampling criterion, resulting in 253 ACCg cells and 90 BLA cells. Figure S1 shows basic characterizations of the single cell activity and example cells with outcome selective responses. As we have previously characterized single-cell encoding of social decision variables within ACCg and BLA in the identical task[6,9], here we mainly focused on determining coordination in frequency and time between ACCg and BLA cells.

To determine whether and how neuronal coordination between BLA and ACCg might underlie social decision-making, we related spiking activity of individual cells from each area with LFP oscillations from the other area by calculating spike-field coherence from pairs of neurons and LFP sites[25,26]. Spike-field coherence values were computed from all recorded cells and LFP sites from which we collected the neural data without any selection criteria. This resulted in 253 ACCg cells paired with 268 BLA LFP sites ($\mathrm{ACCg}_{\mathrm{spike}}$-$\mathrm{BLA}_{\mathrm{field}}$) and 90 BLA cells paired with 257 ACCg LFP sites ($\mathrm{BLA}_{\mathrm{spike}}$-$\mathrm{ACCg}_{\mathrm{field}}$). Particularly, we analyzed coherence during the 150 ms period from the time of acquiring a choice target on free-choice trials (post-decision epoch) and also during the 150 ms period from the central cue onset on forced-choice trials, in order to examine coherence patterns specific to active decisions. Importantly, during this epoch, actors were required to maintain gaze fixation on the target for the duration of the epoch to complete their response, thus removing any eye movement confound and also allowing us to match the timing and gaze-fixation precisely between the free- and forced-choice trials. Crucially, coherence values were always compared in a relative, reward-matched, fashion (i.e., *Other*–*Bottle* for positive ORP, and *Self*–*Both* for negative ORP) such that any observed coherence differences could not be confounded by actors' contingency for receiving a juice reward. That is, actors never received rewards in the *Other*/*Bottle* context, but always received rewards in the *Self*/*Both* context, and the use of the *Other*–*Bottle* and *Self*–*Both* contrasts effectively removes any self-reward contingency within the two independent contexts.

Differences in spike-field coherence between positive ORP (choosing *Other* over *Bottle*, *Other*–*Bottle*) and negative ORP (choosing *Self* over *Both*, *Self*–*Both*) exhibited frequency-specific coordination as a function of the area that contributed spikes in the pair. Spikes from BLA cells and the LFP from ACCg ($\mathrm{BLA_{spike}}$-$\mathrm{ACCg_{field}}$) displayed enhanced coherence in the beta frequency range (defined as 15–25 Hz) for positive ORP ($p < 0.0001$, Wilcoxon sign rank) but suppressed coherence in the same band for negative ORP ($p < 0.0001$) (difference between positive and negative ORPs: $p < 0.0001$, Wilcoxon sign rank; Fig. 3 and Fig. S2;). (Figure 3a, 3c–d, 3f–k show spike-field coherence differences between positive and negative ORPs, whereas Figures 3b, 3e and S2 show spike-field coherence values for each decision preference separately). This enhanced versus suppressed coherence difference was present immediately prior to the time of free-choice decision and lasted until around the time of completing the decision (post-decision epoch). Additionally, in the gamma frequency range (defined as 45–70 Hz), spikes from ACCg cells and LFP from BLA ($\mathrm{ACCg_{spike}}$-$\mathrm{BLA_{field}}$) exhibited enhanced coherence, again, for positive ORP ($p < 0.0001$) but suppressed coherence for negative ORP in the same epoch ($p < 0.0001$) (difference: $p < 0.0001$; Fig. 3d–f). This coherence difference was also present prior to the time of free-choice decision and lasted until the time of completing the decision. However, this time course appeared to be lagged compared to the $\mathrm{BLA_{spike}}$-$\mathrm{ACCg_{field}}$ coherence in the beta band (Fig. 3g; more detail below). Additionally, the differences in spike-field coherence between positive and negative ORPs did not change as a function of the temporal progression within a session, for both $\mathrm{BLA_{spike}}$-$\mathrm{ACCg_{field}}$ (beta band, $p = 0.75$; gamma band, $p = 0.11$, linear regression) and $\mathrm{ACCg_{spike}}$-$\mathrm{BLA_{field}}$ coherence (beta band, $p = 0.47$; gamma band, $p = 0.45$).

Next, we investigated whether the observed spike-field coherence was stronger for the subsets of BLA and ACCg cells that significantly differentiated decision outcomes (*Self*, *Both*, *Other*, *Bottle*; outcome selective cells) (Fig. S1). BLA cells with significant outcome selectivity (37%), exhibited stronger $\mathrm{BLA_{spike}}$-$\mathrm{ACCg_{field}}$ coherence differences between positive and negative ORPs in the post-decision epoch, compared to non-significant cells ($p = 0.02$, Wilcoxon rank sum; Fig. 3h). By contrast, ACCg cells with significant outcome selectivity (36%) did not differ in their $\mathrm{ACCg_{spike}}$-$\mathrm{BLA_{field}}$ coherence differences between the two ORPs than the non-significant counterparts ($p = 0.11$; Fig. 3j). These results suggest that outcome-differentiating cells in BLA may play a more prominent role for the $\mathrm{BLA_{spike}}$-$\mathrm{ACCg_{field}}$ synchrony.

Finally, we performed several control analyses to further confirm the enhanced spike-field coupling between BLA and ACCg for expressing positive ORP. We first examined whether the spike-field coherence patterns were in any way influenced by actors' potential intention to look in the future at either the conspecific's face or the bottle during the inter-trial interval, even though the actors were required to maintain gaze fixation steadily in the main analysis epoch. Specifically, we tested possible differences in all frequency bands during the post-decision epoch on those trials where the actors ultimately looked at the face (compared to no future looking) as well as those trials where they ultimately looked at the bottle (compared to no future looking). For all frequency bands examined, we did not observe marked differences. Crucially, we found no differences in the beta band BLA_{spike}-$ACCg_{field}$ ($p = 0.98$, Wilcoxon rank sum; Fig. 3i) and the gamma band $ACCg_{spike}$-BLA_{field} ($p = 0.94$, Fig. 3k) coherence, supporting that the observed spike-field coherence cannot be explained by potential anticipatory attentional allocation to the conspecific or the bottle. Second, we ruled out several additional factors from explaining our findings. The observed spike-field coherence patterns were not simply driven by changes in spiking activity or LFP powers (Fig. S3, see also Fig. S4 for LFP power temporal evolution in the beta and gamma bands), or by a more global-level synchrony or common input signals by comparing them to field-field coherence patterns (Fig. S5). We also examined whether the between-region spike-field coherence patterns reported here were different from the within-region spike-field coherence patterns and found that they were different in several ways (Fig. S6). Moreover, to test if similar coherence was present even when we construct positive other-regarding and negative other-regarding choices in different ways ('type 2 contrasts'), we contrasted *Both–Self* for delivering rewards to the conspecific and *Bottle–Other* for not delivering rewards to the other monkey. Even with the type 2 contrasts, we found largely consistent spike-field (Fig. S7) and field-field coherence patterns (Fig. S8), indicating that the spike-field coherence is not the mere product of a preferred choice but is driven by positive other-regarding decisions resulting in other's rewards. Finally, we ruled out a possibility that sensory-evoked responses associated with choosing a target stimulus might underlie the differential, frequency-specific, coordination. In both beta and gamma frequency bands, the BLA_{spike}-$ACCg_{field}$ and $ACCg_{spike}$-BLA_{field} coherence patterns were not at all differentially modulated by the onset of a fixation stimulus (Fig. S9). Finally, resampling (75% of randomly selected trials in 1000 iterations to calculate spike-field coherence) produced consistent results, confirming that our results were not driven by outlier cells, sites, or trials (positive versus negative ORPs: BLA_{spike}-$ACCg_{field}$ coherence in the beta band, $p = 0.005$; $ACCg_{spike}$-BLA_{field} coherence in the gamma band, $p = 0.001$; Wilcoxon sign rank). Taken together, these findings support that interareal coherence between BLA and ACCg is enhanced for expressing positive compared to negative ORP.

Crucially, the coordination of spikes and LFP observed between BLA and ACCg was specific to when the actors made decisions (free-choice). Using pseudo-randomly interleaved forced-choice trials in which the computer selected the reward outcomes that were otherwise identical, we constructed spike-field coherence differences with matching reward outcomes in the absence of decision-making. We contrasted *Other-forced* and *Bottle-forced* trials (forced-choice construct of positive ORP) for comparing it to positive ORP and contrasted *Self-forced* and *Both-forced* trials (forced-choice construct of negative ORP) for comparing it to negative ORP. The beta BLA_{spike}-$ACCg_{field}$ coherence as well as the gamma $ACCg_{spike}$-BLA_{field} coherence markedly differed in these comparisons (Fig. 3c, f, and Fig. S2). The beta BLA_{spike}-$ACCg_{field}$ coherence (15–25 Hz), which was selectively enhanced for positive ORP ($p < 0.0001$, Wilcoxon sign rank), was absent for the forced-choice positive ORP ($p = 0.17$) (difference between free-choice and forced-choice: $p < 0.0001$, Wilcoxon rank sum, Fig 3c). Similarly, the gamma $ACCg_{spike}$-BLA_{field} coherence (45–70 Hz), which was again selectively enhanced for positive ORP ($p < 0.0001$), was absent for forced-choice positive ORP ($p = 0.62$) (difference between free-choice and forced-choice: $p < 0.0001$). Therefore, the coordination signatures differentiating positive from negative ORP were unique to making free-choice decisions and not driven by either the visual stimuli or the anticipation of specific reward outcomes.

Given that the beta $\mathrm{BLA_{spike}}$-$\mathrm{ACCg_{field}}$ coherence differences appeared to emerge earlier and terminate sooner than the gamma $\mathrm{ACCg_{spike}}$-$\mathrm{BLA_{field}}$ coherence differences (Fig. 3), we next examined disparities in the coherence onset time to help elucidate any potential functional differences between the two coordination types. The beta $\mathrm{BLA_{spike}}$-$\mathrm{ACCg_{field}}$ coherence began to significantly differentiate positive from negative ORP earlier ($p < 0.05$, Wilcoxon sign rank) than the gamma $\mathrm{ACCg_{spike}}$-$\mathrm{BLA_{field}}$ coherence (Fig. 3g). Additionally, the gamma $\mathrm{ACCg_{spike}}$-$\mathrm{BLA_{field}}$ coherence continued to significantly differentiate positive from negative ORP longer compared to the beta $\mathrm{BLA_{spike}}$-$\mathrm{ACCg_{field}}$ coherence (Fig. 3g). To further investigate temporal profiles, we examined the time at which either spiking or LFP activity began to significantly signal decision outcomes (Fig. S10). Spiking activity associated with choosing *Other* emerged earlier in BLA compared to ACCg ($p = 0.001$; two sample Kolmogorov-Smirnov test). By contrast, there were no such differences for choosing *Self*, *Both*, or *Bottle* outcomes between the areas (all $p = 0.08$) (Fig. S10a). Further, we did not observe any temporal differences in LFP power between the two nodes for both the beta (*Self*, *Both*, *Other*, and *Bottle*, all $p > 0.38$) and the gamma bands (all $p > 0.21$) (Fig. S10b). Finally, we tested if there were any anatomical differences for the coherence strength. We found no discernable anatomical gradients for either the beta or gamma spike-field coherence differences between positive and negative ORPs within ACCg and BLA cells/sites (all comparisons using AP, ML, or Depth dimension separately, or based on principal component analysis; all $|r| < 0.32$, all $p > 0.16$, Spearman correlation).

Directionality of information flow between ACCg and BLA for social decisions

Coordination between ACCg and BLA may exhibit a specific directionality of information flow that may differ between expressing the two ORPs. We performed a partial directed coherence (PDC) analysis, a specialized methodology derived from the Granger principle purposely tailored for analyzing directionality in the frequency-time domain[30]. Without choosing any frequency bands a priori, we observed systematic differences in directional information flow between ACCg and BLA as a function of social decision preference as well as frequency band. We found a significant influence of BLA to ACCg in the beta band (BLA→ACCg) for positive ORP that began around the time of decision and continued for the duration of the post-decision epoch (PDC difference between BLA→ACCg and ACCg→BLA, $p < 0.0001$; Wilcoxon sign rank) (Fig. 4a, b). This increase in directional influence occurred in the same frequency range that exhibited an increase in the $\mathrm{BLA_{spike}}$-$\mathrm{ACCg_{field}}$ coherence for positive ORP. By contrast, we found the opposite pattern for negative ORP, with a stronger influence of ACCg to BLA (PDC difference in the beta band between ACCg→BLA and BLA→ACCg, $p = 0.002$). Similarly, we also found a significant but less pronounced influence of BLA to ACCg in the gamma band (BLA→ACCg) for positive ORP (PDC difference in the gamma band between BLA→ACCg and ACCg→BLA, $p = 0.04$) that appeared later than the BLA→ACCg influence in the beta band (Fig. 4c), again with an opposite influence of ACCg to BLA for negative ORP (PDC difference between ACCg→BLA and BLA→ACCg, < 0.0001). However, while we found frequency-dependent BLA→ACCg influence for positive ORP in the beta and gamma bands (compared to ACCg→BLA), the directionality associated with negative ORP was largely frequency-independent between BLA→ACCg and ACCg→BLA (Fig. 4a, b).

Finally, we observed similar directionality of information flow in both BLA→ACCg and ACCg→BLA for free-choice compared to forced-choice trials for both ORPs (Fig. S11). While we observed a general BLA→ACCg influence in the frequency range encompassing both the beta and low gamma bands for positive ORP, the directionality associated with forced-choice trials was much less frequency-dependent compared to free-choice trials. The directional information flow for negative ORP showed a strong ACCg→BLA influence (again, opposite to the positive ORP) for negative ORP with a longer time span.

Together, these findings demonstrate the presence of specific information flow directions between BLA and ACCg, with a general BLA→ACCg influence for expressing positive ORP and ACCg→BLA influence for expressing negative ORP. Moreover, even though the PDC analyses do not use spikes, the BLA→ACCg information flow for positive ORP was observed in the same beta band that exhibited the enhanced $\mathrm{BLA_{spike}}$-$\mathrm{ACCg_{field}}$ coherence for positive compared to negative ORP.

Decoding social decisions directly from synchrony between ACCg and BLA

To test whether neuronal coordination itself contains decodable information on social decisions, we trained a linear decoder to discriminate decisions directly from spike-field coherence values (Fig. 3). The classifier was trained using randomly selected subsets of 75% of trials and later tested on the remaining 25% of trials used as inputs, yielding estimates of the decision outcome on each trial.

The first decoder was trained to distinguish between *Other* and *Bottle* decisions (positive ORP) from the $\mathrm{BLA_{spike}}$-$\mathrm{ACCg_{field}}$ coherence values in the beta band (15–25 Hz) or from the $\mathrm{ACCg_{spike}}$-$\mathrm{BLA_{field}}$ coherence values in the gamma band (45–70 Hz). Decoding performance from the beta $\mathrm{BLA_{spike}}$-$\mathrm{ACCg_{field}}$ coherence for discriminating *Other* from *Bottle* began to increase prior to the decision time and peaked around the time of the decision ($p < 0.0001$, compared to an empirically derived null distribution, Wilcoxon sign rank) (Fig. 5a). Conversely, the decoding accuracy from the gamma $\mathrm{ACCg_{spike}}$-$\mathrm{BLA_{field}}$ coherence for discriminating *Other* from *Bottle* was lower at the time of free-choice decision but gradually improved during post-decision as monkeys fixated on a chosen option to complete the decision (Fig. 5b). The second decoder was trained to distinguish between *Self* and *Both* for classifying negative ORP in the identical frequency bands and times. Compared to the first decoder, the decoding performance was overall lower (positive vs. negative ORP in the post-decision epoch: $p < 0.0001$ and $p < 0.0001$ for decoding from the $\mathrm{BLA_{spike}}$-$\mathrm{ACCg_{field}}$ and $\mathrm{ACCg_{spike}}$-$\mathrm{BLA_{field}}$ coherence, respectively) and did not show time-locked increases around the time of free-choice decision, albeit still being able to decode above its empirically-derived chance level (Fig. 5a, b). To establish whether improved decoding performance for positive ORP might emerge earlier for the $\mathrm{BLA_{spike}}$-$\mathrm{ACCg_{field}}$ compared to $\mathrm{ACCg_{spike}}$-$\mathrm{BLA_{field}}$ coherence, we divided the epoch into the first and second halves and compared decoding between the two ORPs in each phase (beta $\mathrm{BLA_{spike}}$-$\mathrm{ACCg_{field}}$ vs. gamma $\mathrm{ACCg_{spike}}$-$\mathrm{BLA_{field}}$). In the earlier phase, decoding performance was significantly greater for the beta $\mathrm{BLA_{spike}}$-$\mathrm{ACCg_{field}}$ compared to the gamma $\mathrm{ACCg_{spike}}$-$\mathrm{BLA_{field}}$

coherence ($p < 0.0001$), whereas this relationship was reversed in the later phase, such that relative decoding performance for the gamma ACCg$_{\text{spike}}$-BLA$_{\text{field}}$ was significantly greater than the beta BLA$_{\text{spike}}$-ACCg$_{\text{field}}$ coherence ($p < 0.0001$) (Fig. 5c). These temporal differences in decoding accuracy were consistent with the temporal differences observed between the beta BLA$_{\text{spike}}$-ACCg$_{\text{field}}$ and the gamma ACCg$_{\text{spike}}$-BLA$_{\text{field}}$ coherence differences in favor of positive ORP (Fig. 3g). Although the extent of decoding accuracy for predicting social decisions was low even at the peak level, decoding directly from the synchrony signatures was nevertheless reliable.

Discussion

Distinct neural populations exhibit synchronized activity to possibly facilitate information transmission[25,31]. Evidence supports that interareal oscillatory coordination is one mechanism used to regulate a wide range of functions, from visual perception[32,33], motor planning[34], and spatial navigation[35] to higher-order functions underlying working memory[36], associative learning, and decision-making[37–40]. A number of studies have also emphasized the importance of cortical-subcortical interactions[20,21,24,38–40]. Here, we report that there are specific synchrony signatures of neuronal activity between BLA and ACCg in social decision-making.

Positive ORP was associated with enhanced coherence between spiking of BLA neurons and beta LFP oscillations in ACCg, as well as enhanced coherence between spiking of ACCg neurons and gamma LFP oscillations in BLA. By contrast, negative ORP was associated with suppressed coherence. Thus, enhanced co-engagements of ACCg and BLA may promote positive ORP, whereas co-disengagements may in turn promote negative ORP. Notably, the coordination exhibited frequency specializations. Frequency-specific coordination may provide separate synchrony “streams” that might be useful for communicating different information computed locally from each area. Specializations of beta and gamma frequency channels in processing different cognitive information have been observed in the past for cortico-cortical interactions[41]. Additionally, it has been suggested that the spiking output of BLA synchronizes ACC by influencing oscillations[40]. Our results suggest that beta frequency may link the presynaptic spiking output of BLA cells with the postsynaptic oscillations at the input of ACCg to drive the interareal synchrony in social decision-making.

Synchrony in lower frequency range, including beta, is thought to be more robust and tolerant to temporal dynamics of spiking activity due to slower temporal profiles[42], perhaps making lower frequency more suitable for synchronizing distant structures compared to higher frequency channels like gamma. Further, in some cases, beta synchronization can be short-lived, reflecting momentary anticipation, upcoming decisions, and internally driving choices in a top-down manner[43]. A synchronization between BLA spikes and ACCg field may facilitate robust and long-range coordination. Recently, accumulating evidence supports a role of beta synchronization in decision-making, especially when decisions involve context-specific and subjective processes[44]. The increase in beta synchrony between BLA spikes and ACCg field during post-decision may therefore signify subjective decision-related feedback associated with positive ORP. Conversely, synchrony in higher frequency is likely be driven by local computations requiring fast-spiking GABA-ergic interneurons[42,45]. Gamma frequency has been implicated in generating selective representations of salient stimuli over others[46]. The gamma coherence between ACCg spikes and BLA field may indicate further local computations in ACCg following the long-range synchrony initiated by BLA and may support communicating additional agent-specific computations linked to vicarious reward in ACCg[6].

The directionality of information was largely selective for positive ORP, with the predominant directional influence from BLA to ACCg in the beta frequency greater for positive compared to negative ORP. This directionality occurred in the same frequency that exhibited enhanced coordination between BLA spikes and ACCg field for positive ORP. Crucially, the $\mathrm{BLA}_{\mathrm{spike}}$-$\mathrm{ACCg}_{\mathrm{field}}$ coordination associated with positive ORP was amplified for the outcome selective BLA cells. Taking these results together with earlier emergence of the $\mathrm{BLA}_{\mathrm{spike}}$-$\mathrm{ACCg}_{\mathrm{field}}$ compared to the $\mathrm{ACCg}_{\mathrm{spike}}$-$\mathrm{BLA}_{\mathrm{field}}$ coordination, BLA cells that differentiate social decision outcomes may engage ACCg for positive ORP. BLA cells also signal social contextual information, such as social gaze orientations and facial expressions[47,48]. Future work can test if and when BLA cells with other known functions transmit information to rostral ACCg or other medial prefrontal cortical areas to bias social decisions. Further, optogenetic tools would help causally test the function of BLA-ACCg synchrony in social decision-making.

Notably, the BLA-ACCg synchrony was largely specific to active decision-making, compared to trials on which the computer made the decisions, supporting that the interareal synchrony was not simply driven by anticipation of upcoming reward outcomes. Although it is inherently difficult to entirely rule out the possibility that these circuits are less engaged by virtue of not making active decisions, expressing social preference may engage these circuits in unique ways. This hypothesis is supported by two previous observations in the primate BLA demonstrating specialized codes for computing free-choice, compared to forced-choice, decisions[9,49].

In social decision-making, it is imperative to be aware of a chosen option and an ultimate actualization of the reward outcome for either self or other. In the reinforcement learning theory, post-decision, decision-trace, or ‘afterstate’ signals available during post-decisional monitoring can serve as an important and unique feedback mechanism for efficient learning of actions and reward outcomes[50]. The observed spike-field coherence is unlikely to be directly involved in generating a decision as the coherence emerged after a stage of formulating a choice for both the beta and gamma bands. Additionally, the increase in the coherence in both bands specific to positive ORP only remained until when a potential reward could be received, displaying a temporal specificity to the post-decision epoch. We therefore hypothesize that BLA and ACCg interact during a post-decision state associated with expressing positive ORP. These synchronous interactions in the prefrontal-amygdala circuits, known for incorporating social, affective, and reward information, may occur as a result of synchronized feedback useful for adjusting future social decisions. Future work with a specific behavioral design for modulating the fidelity of post-decision monitoring in relation to BLA-ACCg synchrony is necessary to directly test this hypothesis.

Finally, it is worth pointing out some limitations of our work. Although the task had an embedded condition for delivering juice to a non-social entity (bottle), it remains unknown whether similar coherence would be present during a completely non-social context (despite the fact that the coherence was specific to other's reward outcome, rather than preference per se; Fig. S7). Future work should examine how coherence might be differentially modulated between social and non-social contexts. Moreover, despite the fact that we removed any self-reward contingency within the two independent decision-making contexts (*Self–Both* from *Self/Both* context and *Other–Bottle* from *Other/Bottle* context), it is worthwhile to acknowledge that the two contexts were still different and deriving positive ORP from *Other/Bottle* context and negative ORP from *Self/Both* context might have influenced our findings. However, the fact that we observed overwhelmingly similar spike-field as well as field-field coherence upon deriving positive ORP from the *Self/Both* context (*Both–Self*) and negative ORP from the *Other/Bottle* context (*Bottle–Other*) greatly mitigates this concern.

Overall, our findings support that BLA and ACCg neurons utilize distinct frequency channels and direction-selective coordination in social decision-making. Efficient and strategic coordination occurring between medial prefrontal regions and the amygdala that prioritizes positive over negative ORP may play an essential role in promoting mutually beneficial social cohesion. In turn, failures in synchronized transmissions along the prefrontal-amygdala network may bias the network to converge toward producing atypical social behaviors.

Online Methods

Animals

Two adult male rhesus macaques (*Macaca mulatta*) were involved in the study as actors (monkeys K and H; ages, both 6; weights, 7 and 8 kg), and two adult female monkeys (ages, 6 and 10; weights, 9 and 10 kg) were involved only as recipients in the social reward allocation task. All animals were unrelated and not cagemates. Actors were housed in a colony room with other male macaques, whereas two female macaques resided in an adjacent colony room with other females. All four subjects were housed in pairs with other animals from the colony, kept on a 12-hr light/dark cycle, had unrestricted access to food, and controlled access to fluid during testing. No animals were excluded from our analyses. All procedures were approved by the Yale Institutional Animal Care and Use Committee and in compliance with the National Institutes of Health Guide for the Care and Use of Laboratory Animals.

Surgery and anatomical localization

All four animals received a surgically implanted headpost (Grey Matter Research) for restraining their head during the experiments. Subsequently, a second surgery was performed on actor monkeys to implant a recording chamber (Crist) to provide access to ACCg and BLA. Placement of the chambers were guided by both structural magnetic resonance imaging (MRI, 3T Siemens) scan and stereotaxical coordinates. Prior to starting the recording experiments, we performed a manganese (Mn)-enhanced magnetic resonance imaging (MEMRI) session for each actor monkey to precisely localize our recording sites in both ACCg and BLA. For MEMRI, we focally infused 2 μl of 19.8 μg/μl of Mn (manganese (II) chloride) in saline solution in both areas using modified Hamilton syringes that traveled along the identical trajectory as our electrodes. We then performed a structural MRI scan 3 hours after the infusion to visualize a bright halo to confirm anatomical locations[51]. All electrophysiological recordings were carried out simultaneously from ACCg (Brodmann areas 24a, 24b, and 32)[29] and BLA[29] (Fig. 2).

Social reward allocation task

Two monkeys (an actor and a recipient) sat in primate chairs (Precision Engineering, Inc.) at 100 cm from one another at a 90° angle (Fig. 1a). Each monkey had his own monitor, which displayed identical visual stimuli. Both monkeys had their own juice tubes from which juice drops were delivered via solenoid valves. A third juice tube with its own dedicated solenoid valve delivered juice rewards into an empty bottle (*Bottle*), which was placed on the opposite side of the recipient (Fig. 1a). To prevent monkeys from forming secondary associations of solenoid clicks, the three solenoid valves were placed in another room and white noise was played in the background during all experimental sessions. An infrared eye-tracking camera (EyeLink 1000, SR Research) continuously recorded the horizontal and vertical eye positions from actor monkeys.

An actor began a trial by fixating on a central square for 150 ms with gaze. The reward value at stake on each trial was specified by a magnitude cue displayed as a vertical bar indicating juice volume (0.2, 0.4, or 0.6 ml). The actor was required to maintain gaze fixation on the magnitude cue for 400 ms. Following a variable delay (200, 400, or 600 ms), the actor was presented with either a free-choice (75%) or a forced-choice (25%) trial. On free-choice trials, two visual targets appeared at two random peripheral locations on opposite sides of the screen. The actor had 2 sec to make a choice by shifting gaze to a target and maintaining the fixation on the target for additional 150 ms in order to complete a choice (i.e., any break in gaze fixation resulted in an incomplete trial with no further progression into the trial). These choice targets were always presented in two distinct contexts presented pseudo-randomly. In the *Self*/*Both* context (50% of free-choice trials), the actor made decisions to deliver a juice drop to himself (*Self*) or both himself and the recipient monkey (*Both*; the same amount was delivered at the same time to both monkeys). By contrast, in the *Other*/*Bottle* context (50% of free-choice trials), the actor made decisions to deliver a juice drop to the recipient monkey (*Other*) or to the empty juice collection bottle (*Bottle*). Critically, any choice made in the two contexts were ‘reward-matched’ from actor’s perspective such that the actor always received a reward in the *Self*/*Both* context but never received a reward in the *Other*/*Bottle* context. After a following variable delay from completing the decision (200, 400, 600, or 800 ms), a juice reward corresponding to the chosen target was delivered to himself (*Self*), to the recipient (*Other*), to both monkeys (*Both*), or to the bottle (*Bottle*). On forced-choice trials, only a single central cue was presented on the screen, and the actor had to simply maintain the fixation for 150 ms to complete the forced-choice decision (i.e., any break in fixation resulted in an incomplete trial with no further progression into the trial). These computer-determined reward outcomes occurred with equal frequency, pseudorandomly ordered. After a following variable delay (200, 400, 600, or 800 ms), a juice reward corresponding to the central cue was delivered to himself (*Self-forced*), to the recipient (*Other-forced*), to both monkeys (*Both-forced*), or to the bottle (*Bottle-forced*). For both free-choice and forced-choice trials, reward delivery was followed by a 2.5 sec inter-trial interval, during which the actor was free to look at the recipient or any other locations in the setup. A trial was considered incomplete if the actor failed to choose a target or maintain the required 150 ms fixation on free-choice trials or to maintain the required 150 ms fixation on the cue on forced-choice trials. The incomplete trials were not included in the analyses.

Electrophysiology

LFP and spiking activity was recorded using 16-channel axial array electrodes (U- or V-Probes, Plexon) or single tungsten electrodes (FHC Instruments) placed in each of the recording regions using a 32-channel system (Plexon). At the beginning of each session, a guide tube was used to penetrate the intact dura and to guide electrodes, which were lowered using a motorized multi-electrode microdrive system (NaN Instruments) with a speed of 0.02 mm/sec. After the electrodes reached the target sites in both ACCg and BLA, we waited 30 min for the tissue to settle before starting each recording session to ensure signal stability. Because some of the data were obtained using two 16-channel electrode arrays, one in ACCg and the other in BLA (20% of the total recording sessions), we randomly assigned 16 uniquely paired LFP sites between the two regions, using a random number generator, to remove redundant inflations of correlation for the relevant data. Otherwise, no cells or LFP sites were excluded from our analyses.

Data Analysis

See Data and Code Availability information at the end of the Online Method section.

Behavioral analyses

We constructed a choice preference index as contrast ratios[6,27,28,52] (Eq. 1).

$$Preference\ Index = \frac{R_a - R_b}{R_a + R_b} \qquad \text{(Eq. 1)}$$

R_a and R_b were the frequency of particular choices. For the *Self*/*Both* context, R_a and R_b were numbers of *Both* and *Self* choices, respectively. For the *Other*/*Bottle* context, R_a and R_b were numbers of *Other* and *Bottle* choices, respectively. An index of 1 thus corresponds to always choosing a positive ORP outcome, –1 corresponds to always choosing a negative ORP outcome, and 0 indicates indifference. We additionally performed a regression analysis to quantify changes over time in their behavioral preferences for both *Self*/*Both* and *Other*/*Bottle* context in each session.

Looking frequency was computed based on the average number of gaze shifts landing on the face of the recipient monkey (the face region of the recipient was empirically mapped and fitted with a rectangle window) or the bottle (mapped empirically with the same-dimensioned window as the face region) during the 2.5 sec inter-trial interval[6,27,28,52].

Decision reaction time, the time from the onset of two targets on free-choice trials to eye movement onset, were computed using a 20° $\sec^{-1}$ velocity criterion[6,27,28,52].

Spiking and LFP activity

Broadband analog signals were amplified, band-pass filtered (250 Hz–8 kHz), and digitized (40 kHz) using a Plexon OmniPlex system. Spiking data were saved for waveform verifications offline and automatically sorted using the MountainSort algorithm[53]. LFP data were analyzed using custom MATLAB scripts (The MathWorks) and the Chronux signal processing toolbox[54]. Continuous LFP signals from each recording electrode in each area were segmented into 1-sec periods centered on acquiring (i.e. saccade offset) the choice target or acquiring the central cue at a sample rate of 1 kHz. Raw signals were then band-passed filtered from 2.5 Hz to 250 Hz. We chose a zero-phase filter to avoid introducing phase-distortions to the signals. Signals were normalized by subtracting a reference voltage trace recorded from an independent reference electrode placed in the subdural space in order to eliminate the common noise from each electrode. In a subset of the data where we could accurately compare bipolar and unipolar referencing methods (using 16-channel electrode arrays in both ACCg and BLA; 20% of the total recording sessions), we found similar spike-field coherence results as well as PDC directional results between the two methods (see ref [55]). Three primary epochs were used to carry out neural data analyses: during the 150 ms window during the first fixation period required to begin each trial (baseline epoch); during the 150 ms period from the time of acquiring (i.e. saccade offset) a choice target on free-choice trials (post-decision epoch) and also during the 150 ms period after the central cue onset on forced-choice trials (cue epoch). To determine outcome selective cells from each region, we performed one-way ANOVA with outcome as the factor (*Self*, *Both*, *Other*, *Bottle*) using the spiking activity from either the post-decision epoch or reward epoch (50–450 ms from reward onset). Finally, to compare the emergence times of outcome selective signals in both spiking and LFP activity, we calculated the cumulative distributions of the times at which each cell or LFP site exhibited significant encoding of different outcomes around the time of decision-making, relative to the baseline epoch ($p < 0.05$, Wilcoxon sign rank).

Spike-field coherence and field-field coherence

We quantified spike-field coherence level by examining the phase differences between LFP and spike signals. We designated one area as the “spike contributor” and the other area as the “field contributor”. Spike-field coherence was calculated from two directions, either ACCg or BLA as the spike contributor and the other area in the pair as the field contributor. We first binned spikes and LFP using sliding time windows of 150 ms, in steps of 50 ms, for a 1 sec interval centered on the time of decision on free-choice trials or the cue onset on forced-choice trials. Fourier estimates were then computed by means of a multi-taper transformation applied to single trial data; we selected a time half-bandwidth product of 2, and multiplied the raw signals by 3 Slepian (orthogonal) tapers[56]. With a 1 kHz sampling rate, this yielded a frequency resolution of ~3.096 Hz. Spectral density estimates were additionally restricted to the 10–80 Hz interval, considering the Nyquist limit. The spectrum density of point process (spikes) was transformed by applying fast Fourier transform on the discrete data. Coherence was then calculated between two spectrum densities of continuous process (LFP) and point process (spikes) by computing the cross-spectral density of the two processes (x and y; P_{xy}) with respect to frequency (f), which was normalized by the product of the power spectral densities of each process (P_{xx} and P_{yy}) as a function of frequency (Eq. 2).

$$Coherence = \frac{|P_{xy}(f)|^2}{P_{xx}(f)P_{yy}(f)} \quad \text{(Eq. 2)}$$

Raw coherence values therefore ranged from 0 to 1, where a perfectly constant phase relationship between the two regions would be indicated by a coherence value of 1 while an absence of any phase relationship would be indicted by a value of 0. We contrasted coherence values between different conditions and obtained average over pairs of cells and LFP sites, where the spike contributor had at least 1 spike in a 150-ms bin. A linear regression was used to quantify the changes in $\text{BLA}_{\text{spike}}$-$\text{ACCg}_{\text{field}}$ coherence and $\text{ACCg}_{\text{spike}}$-$\text{BLA}_{\text{field}}$ coherence patterns for both the beta and gamma band over time within each session.

For calculating within-region spike-field coherence, we used the same approach described above for between-region spike-field coherence but excluded relating spikes and LFPs originating from the same electrode channels. For looking at the relationships of LFPs between the two regions, field-field coherence was computed in the same format as in the spike-field coherence described above except the following. Field-field coherence was calculated between two spectrum densities of continuous processes (LFPs from each region) by computing the cross-spectral density of the two processes (x and y; P_{xy}) with respect to frequency (f), which was normalized by the product of the power spectral densities of LFP processes from each region (P_{xx} and P_{yy}) with respect to frequency (same format as in Eq. 2).

Directionality of information flow

We calculated partial directed coherence (PDC), which is based on multivariate autoregressive (MVAR) model and is well suited for describing directionality of information flow between simultaneously recorded time series in the frequency domain[30]. We contrasted time-varying PDC as (*Other*) – (*Bottle*) and (*Self*) – (*Both*) for free-choice trials, as well as (*Other-forced*) – (*Bottle-forced*) and (*Self-forced*) – (*Both-forced*) for forced-choice trials. As we did for the coherence analyses, we restricted the combinations of pairs to be unique over sites. For example, for the data recorded from a 16-channel array placed in each of the two areas, we randomly selected 16 unique pairs out of 16 × 16 pairs to avoid redundancy and undesired inflation in correlations. For each pairwise LFP signals, the parameters of multivariate autoregressive model (MVAR) of order r was formulated as:

$$A_r = \begin{bmatrix} a_{ii}^r & a_{ij}^r \\ a_{ji}^r & a_{jj}^r \end{bmatrix} \quad \text{(Eq. 3)}$$

where parameter a reflects linear relationship between channel i and j at delay r. While $r = 1 \ldots p$ represents the order of the model. To obtain PDC measures over time, instead of applying adaptive filtering method to estimate time-varying autoregressive coefficient, we calculated PDC values based on sliding window of 150 ms with a 50 ms step size just as we do for the coherence measures. Model order of MVAR model was estimated by using the post-decision epoch data to minimize Schwarz Bayesian information criteria (SBC) for all LFP pairs. This resulted in p = 12, specifying that the current value is predicted by immediately preceding twelve values in the series. The model extended to the frequency dimension was defined as:

$$A\left(f\right) = I - \sum_{r=1}^{p} A_r Z^{-r}|_{z=e^{j2\pi f}} \quad \text{(Eq. 4)}$$

where I is the identity matrix and f ranges within 0 to Nyquist frequency. PDC values were then defined by taking the absolute value of $A(f)$ and normalizing by its column vector (see equation 18 in reference 30). To reduce the co-variability of signal between channels due to common sources, we adapted the extended version of classical PDC[57]. The new generalized orthogonalized measure of PDC ($\widetilde{\psi}$) as a function of time and frequency was defined as:

$$\widetilde{\psi_{ij}}(f) = \frac{1}{\lambda_{kk}^2}\frac{|Real\{A_{ij}(f)\}|}{\sqrt{a_j^H(f)\Sigma_w^{-1}a_j(f)}} \cdot \frac{|Imag\{A_{ij}(f)\}|}{\sqrt{a_j^H(f)\Sigma_w^{-1}a_j(f)}}, \quad i \neq j \quad \text{(Eq. 5)}$$

where a_j is the j's column vector and A_{ij} is the ijth element of $A(f)$. H denotes the Hamilton transpose of the vector a. Σ_w is the diagonal covariance matrix from MVAR noise covariance matrix w, where λ_{kk} is a diagonal element of Σ_w. For one pair of channels, ($\widetilde{\psi}$) was shown in a 2 × 2 matrix, where non-diagonal elements represent directional interaction between channel i and j, that is, ACCg→BLA or BLA→ACCg. We then calculated and averaged ($\widetilde{\psi}$) for all trials in each condition (*Self*, *Both*, *Other*, or *Bottle*) and averaged pairwise sites of PDC for all recording sessions. For testing whether specific frequency bands exhibit significantly different PDC values between conditions for each ACCg→BLA and BLA→ACCg, we compared PDC values from the same time window used for the main spike-field coherence results.

Linear Discriminant analysis (LDA)

To test the decodability of social decisions directly from spike-field coherence values, we used a standard linear classifier for population decoding[58]. The analysis was run separately for each time-frequency bin (150 ms bin with 5 ms steps) and for each decision context. For a given time-frequency bin and context, the trial-level vector of spike-field coherence values in that bin was extracted, along with the corresponding vector of decision outcomes for each trial. This outcome vector contained *Other* and *Bottle* labels or *Self* and *Both* labels, depending on the decision context. The decoder was therefore trained to discriminate between binary outcomes on the basis of spike-field coherence values. In the training phase, 75% of trials were selected at random to train the classifier model. In the testing phase, coherence values for the remaining 25% of trials were used as inputs, yielding estimates of the decision outcome on each trial.

Decoder performance was assessed as the percentage of test-phase trials that were correctly labeled. The statistical significance of the performance was assessed with a permutation test.

For each of 100 iterations, a null value of the decoder's performance was obtained by shuffling the decision outcome labels before training and testing. The analysis thus produced arrays of matching sizes representing the real and null decoding performance for each (time, frequency, condition, iteration) sequence. Decoding was considered significant if the average performance was higher than the corresponding null performance at least 99% of the time ($p < 0.01$, FDR-corrected for multiple comparisons over frequencies).

General and statistical statements

See *Life Sciences Reporting Summary* for consistency and transparency in reporting. Data collection and analysis were not performed blind to the conditions of the experiments. Data collection was randomized for all trial types and stimulus presentations but had no experimental grouping based on animals. Statistical tests included parametric and non-parametric methods. For both parametric and non-parametric tests, data were well-distributed with respect to the assumptions of the test, but this was not formally tested. For tests involving an empirically derived null distribution, the number of iterations and shuffling / resampling procedures were consistent with those of previous publications (e.g., ref [11]). No statistical methods were used to pre-determine sample sizes but our sample sizes (both behavioral and neuronal) are similar to those reported in previous publications (e.g., refs [6,34,41]).

Data availability

Behavioral and neural data presented in this paper are available at https://github.com/changlabneuro/medial-prefrontal-amygdala-coordination-analyses.

Code availability

Behavioral and neural data analysis codes central to this paper are available at https://github.com/changlabneuro/medial-prefrontal-amygdala-coordination-analyses.

Supplementary Material

Refer to Web version on PubMed Central for supplementary material.

Acknowledgements

We are extremely grateful to Bijan Pesaran for his guidance on examining oscillatory neural processes throughout the duration of this research. We especially thank Daeyeol Lee and Alex Kwan for their thoughtful discussions and suggestions on improving this work. We also thank Amrita Nair and Siqi Fan for insightful comments on the manuscript. This work was supported by the National Institute of Mental Health (R01MH110750; R01MH120081; R21MH107853; R00MH099093), Alfred P. Sloan Foundation (FG-2015-66028), and the Teresa Seessel Postdoctoral Fellowship.

References

1. Behrens TEJ, Hunt LT & Rushworth MFS The computation of social behavior. Science 324, 1160–1164 (2009). [PubMed: 19478175]
2. Bhanji JP & Delgado MR The social brain and reward: social information processing in the human striatum. Wiley Interdiscip. Rev. Cogn. Sci 5, 61–73 (2014). [PubMed: 24436728]
3. Sliwa J & Freiwald WA A dedicated network for social interaction processing in the primate brain. Science 356, 745–749 (2017). [PubMed: 28522533]

4. Ruff CC & Fehr E The neurobiology of rewards and values in social decision making. Nat. Rev. Neurosci 15, 549–562 (2014). [PubMed: 24986556]
5. Seo H & Lee D Neural basis of learning and preference during social decision-making. Curr. Opin. Neurobiol 22, 990–995 (2012). [PubMed: 22704796]
6. Chang SWC, Gariépy J-F & Platt ML Neuronal reference frames for social decisions in primate frontal cortex. Nat. Neurosci 16, 243–250 (2013). [PubMed: 23263442]
7. Haroush K & Williams ZM Neuronal prediction of opponent's behavior during cooperative social interchange in primates. Cell 160, 1233–1245 (2015). [PubMed: 25728667]
8. Noritake A, Ninomiya T & Isoda M Social reward monitoring and valuation in the macaque brain. Nat. Neurosci 21, 1452–1462 (2018). [PubMed: 30224807]
9. Chang SWC et al. Neural mechanisms of social decision-making in the primate amygdala. Proc. Natl. Acad. Sci. U. S. A 112, 16012–16017 (2015). [PubMed: 26668400]
10. Grabenhorst F, Báez-Mendoza R, Genest W, Deco G & Schultz W Primate amygdala neurons simulate decision processes of social partners. Cell 177, 986–998.e15 (2019). [PubMed: 30982599]
11. Munuera J, Rigotti M & Salzman CD Shared neural coding for social hierarchy and reward value in primate amygdala. Nat. Neurosci 21, 415–423 (2018). [PubMed: 29459764]
12. Azzi JCB, Sirigu A & Duhamel J-R Modulation of value representation by social context in the primate orbitofrontal cortex. Proc. Natl. Acad. Sci 109, 2126–2131 (2012). [PubMed: 22308343]
13. Baez-Mendoza R, Harris CJ & Schultz W Activity of striatal neurons reflects social action and own reward. Proc. Natl. Acad. Sci 110, 16634–16639 (2013). [PubMed: 24062436]
14. Falcone R, Brunamonti E, Ferraina S & Genovesio A Neural encoding of self and another agent's goal in the primate prefrontal cortex: human-monkey interactions. Cereb. Cortex 26, 4613–4622 (2016). [PubMed: 26464474]
15. Nummela SU, Jovanovic V, Mothe L, de la & Miller CT Social context-dependent activity in marmoset frontal cortex populations during natural conversations. J. Neurosci 37, 7036–7047 (2017). [PubMed: 28630255]
16. Apps MAJ, Rushworth MFS & Chang SWC The anterior cingulate gyrus and social cognition: tracking the motivation of others. Neuron 90, 692–707 (2016). [PubMed: 27196973]
17. Hill MR, Boorman ED & Fried I Observational learning computations in neurons of the human anterior cingulate cortex. Nat. Commun 7, 12722 (2016). [PubMed: 27598687]
18. Zaki J & Ochsner K The neuroscience of empathy: progress, pitfalls and promise. Nat. Neurosci 15, 675–680 (2012). [PubMed: 22504346]
19. Mars RB et al. On the relationship between the "default mode network" and the "social brain". Front. Hum. Neurosci 6, (2012).
20. Amadei EA et al. Dynamic corticostriatal activity biases social bonding in monogamous female prairie voles. Nature 546, 297–301 (2017). [PubMed: 28562592]
21. Allsop SA et al. corticoamygdala transfer of socially derived information gates observational learning. Cell 173, 1329–1342.e18 (2018). [PubMed: 29731170]
22. Zhan Y et al. Deficient neuron-microglia signaling results in impaired functional brain connectivity and social behavior. Nat. Neurosci 17, 400–406 (2014). [PubMed: 24487234]
23. Carmichael ST & Price JL Limbic connections of the orbital and medial prefrontal cortex in macaque monkeys. J. Comp. Neurol 363, 615–641 (1995). [PubMed: 8847421]
24. Klavir O, Genud-Gabai R & Paz R Functional connectivity between amygdala and cingulate cortex for adaptive aversive learning. Neuron 80, 1290–1300 (2013). [PubMed: 24314732]
25. Pesaran B et al. Investigating large-scale brain dynamics using field potential recordings: analysis and interpretation. Nat. Neurosci 21, 903 (2018). [PubMed: 29942039]
26. Fries P A mechanism for cognitive dynamics: neuronal communication through neuronal coherence. Trends Cogn. Sci 9, 474–480 (2005). [PubMed: 16150631]
27. Chang SWC, Winecoff AA & Platt ML Vicarious reinforcement in rhesus macaques (Macaca mulatta). Front. Neurosci 5, (2011).

28. Chang SWC, Barter JW, Ebitz RB, Watson KK & Platt ML Inhaled oxytocin amplifies both vicarious reinforcement and self reinforcement in rhesus macaques (Macaca mulatta). Proc. Natl. Acad. Sci 109, 959–964 (2012). [PubMed: 22215593]
29. Paxinos G, Huang X-F & Toga AW The Rhesus Monkey Brain in Stereotaxic Coordinates. (Academic Press, 1999).
30. Baccalá LA & Sameshima K Partial directed coherence: a new concept in neural structure determination. Biol. Cybern 84, 463–474 (2001). [PubMed: 11417058]
31. Buzsáki G & Wang X-J Mechanisms of gamma oscillations. Annu. Rev. Neurosci 35, 203–225 (2012). [PubMed: 22443509]
32. Hipp JF, Engel AK & Siegel M Oscillatory synchronization in large-scale cortical networks predicts perception. Neuron 69, 387–396 (2011). [PubMed: 21262474]
33. Womelsdorf T, Fries P, Mitra PP & Desimone R Gamma-band synchronization in visual cortex predicts speed of change detection. Nature 439, 733–736 (2006). [PubMed: 16372022]
34. Wong YT, Fabiszak MM, Novikov Y, Daw ND & Pesaran B Coherent neuronal ensembles are rapidly recruited when making a look-reach decision. Nat. Neurosci 19, 327–334 (2016). [PubMed: 26752158]
35. Kahana MJ, Sekuler R, Caplan JB, Kirschen M & Madsen JR Human theta oscillations exhibit task dependence during virtual maze navigation. Nature 399, 781–784 (1999). [PubMed: 10391243]
36. Fujisawa S & Buzsáki GA 4 Hz oscillation adaptively synchronizes prefrontal, VTA, and hippocampal activities. Neuron 72, 153–165 (2011). [PubMed: 21982376]
37. Adhikari A, Topiwala MA & Gordon JA Synchronized activity between the ventral hippocampus and the medial prefrontal cortex during anxiety. Neuron 65, 257 (2010). [PubMed: 20152131]
38. Antzoulatos EG & Miller EK Increases in functional connectivity between prefrontal cortex and striatum during category learning. Neuron 83, 216–225 (2014). [PubMed: 24930701]
39. Brincat SL & Miller EK Frequency-specific hippocampal-prefrontal interactions during associative learning. Nat. Neurosci 18, 576–581 (2015). [PubMed: 25706471]
40. Taub AH, Perets R, Kahana E & Paz R Oscillations synchronize amygdala-to-prefrontal primate circuits during aversive learning. Neuron 97, 291–298.e3 (2018). [PubMed: 29290553]
41. Buschman TJ & Miller EK Top-down versus bottom-up control of attention in the prefrontal and posterior parietal cortices. science 315, 1860–1862 (2007). [PubMed: 17395832]
42. Engel AK, Fries P & Singer W Dynamic predictions: oscillations and synchrony in top-down processing. Nat. Rev. Neurosci 2, 704–716 (2001). [PubMed: 11584308]
43. Engel AK & Fries P Beta-band oscillations--signalling the status quo? Curr. Opin. Neurobiol 20, 156–165 (2010). [PubMed: 20359884]
44. Spitzer B & Haegens S Beyond the status quo: a role for beta oscillations in endogenous content (re)activation. eNeuro 4, (2017).
45. Cardin JA et al. Driving fast-spiking cells induces gamma rhythm and controls sensory responses. Nature 459, 663–667 (2009). [PubMed: 19396156]
46. Jia X & Kohn A Gamma rhythms in the Brain. PLOS Biol. 9, e1001045 (2011). [PubMed: 21556334]
47. Livneh U, Resnik J, Shohat Y & Paz R Self-monitoring of social facial expressions in the primate amygdala and cingulate cortex. Proc. Natl. Acad. Sci 109, 18956–18961 (2012). [PubMed: 23112157]
48. Gothard KM, Battaglia FP, Erickson CA, Spitler KM & Amaral DG Neural responses to facial expression and face identity in the monkey amygdala. J. Neurophysiol 97, 1671–1683 (2007). [PubMed: 17093126]
49. Grabenhorst F, Hernádi I & Schultz W Prediction of economic choice by primate amygdala neurons. Proc. Natl. Acad. Sci 109, 18950–18955 (2012). [PubMed: 23112182]
50. Sutton RS & Barto AG Reinforcement Learning: An Introduction. (A Bradford Book, 1998).

References appearing only in the Methods

51. Liu Y, Yttri EA & Snyder LH Intention and attention: different functional roles for LIPd and LIPv. Nat. Neurosci 13, 495–500 (2010). [PubMed: 20190746]
52. Chang SW et al. Neural mechanisms of social decision-making in the primate amygdala. Proc. Natl. Acad. Sci 112, 16012–16017 (2015). [PubMed: 26668400]
53. Chung JE et al. A fully automated approach to spike sorting. Neuron 95, 1381–1394.e6 (2017). [PubMed: 28910621]
54. Bokil H, Andrews P, Kulkarni JE, Mehta S & Mitra PP Chronux: a platform for analyzing neural signals. J. Neurosci. Methods 192, 146–151 (2010). [PubMed: 20637804]
55. Bastos AM & Schoffelen J-M A tutorial review of functional connectivity analysis methods and their interpretational pitfalls. Front. Syst. Neurosci 9, 175 (2015). [PubMed: 26778976]
56. Jarvis MR & Mitra PP Sampling properties of the spectrum and coherency of sequences of action potentials. Neural Comput. 13, 717–749 (2001). [PubMed: 11255566]
57. Omidvarnia AH et al. Orthogonalized partial directed coherence for functional connectivity analysis of newborn EEG in Neural Information Processing (eds. Huang T, Zeng Z, Li C & Leung CS) 683–691 (Springer Berlin Heidelberg, 2012).
58. Saez A, Rigotti M, Ostojic S, Fusi S & Salzman CD Abstract context representations in primate amygdala and prefrontal cortex. Neuron 87, 869–881 (2015). [PubMed: 26291167]

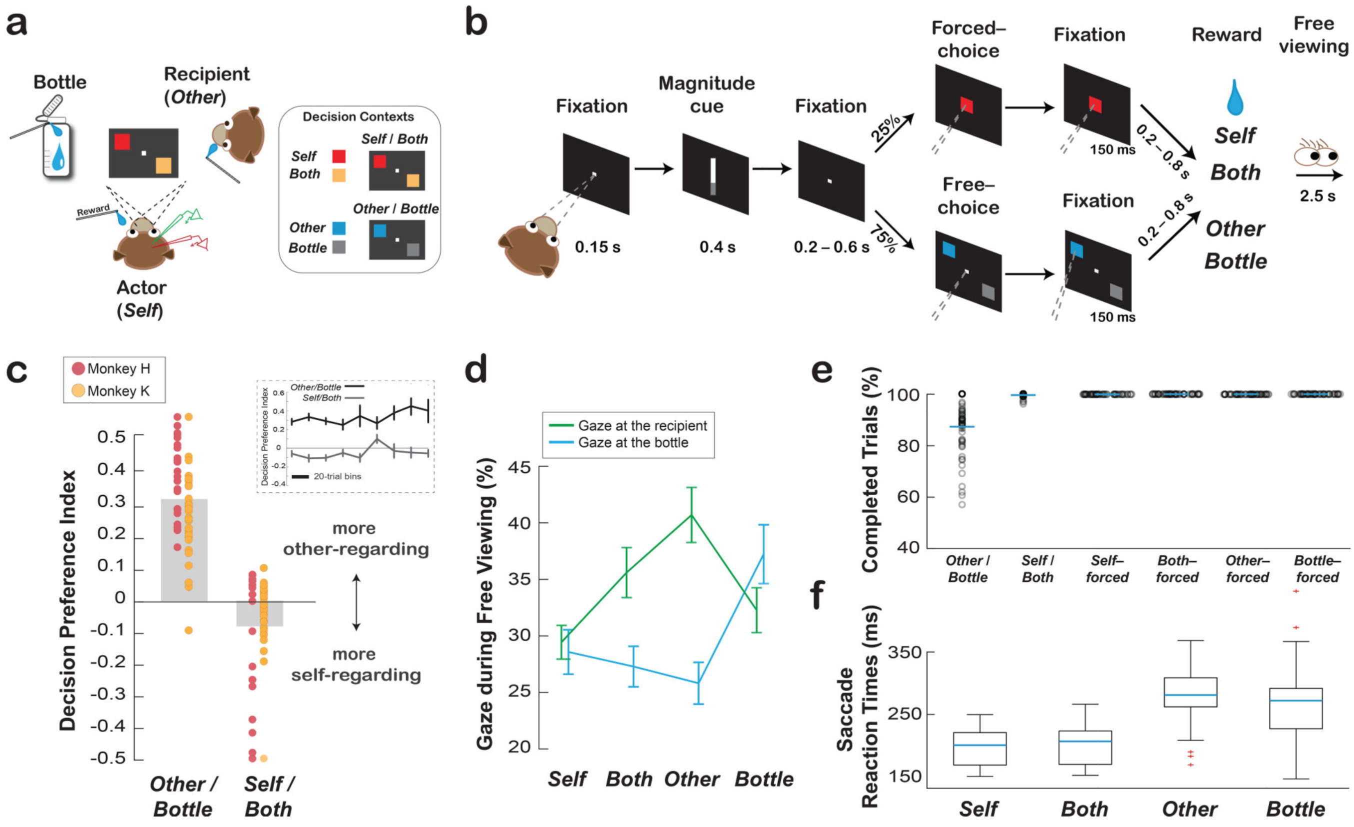

Fig. 1. Social reward allocation task and the behaviors associated with social decision preference.
(**a**) Experimental setting involving an actor monkey, a recipient monkey, and an operating juice collection bottle. The inset shows example stimulus-reward outcome mappings for the two distinct contexts for rewarding the actor (*Self*) or both the actor and the recipient (*Both*) (*Self*/*Both* context), and for rewarding the recipient (*Other*) or the bottle (*Bottle*) (*Other*/*Bottle* context). (**b**) Task sequence for the social reward allocation task (Online Methods). (**c**) Monkeys exhibited context-dependent positive and negative ORPs. Decision preferences are expressed as averaged contrast ratios for the two decision contexts. Data points overlaid on top show the biases for all individual sessions for each subject (mean ± s.e.m., n = 57 sessions). The inset shows the preferences over time for each context (mean ± s.e.m., 57 sessions). (**d**) Social gaze patterns reflected decisions to deliver juice rewards to the recipient or the bottle as a function of different decisions. Shown are the mean (± s.e.m., 57 sessions) proportions of gaze to the recipient or to the bottle during the free viewing period for each reward outcome. (**e**) Average proportions of completed free-choice trials for *Other*/*Bottle* and *Self*/*Both* contexts and completed forced-choice trials for choosing *Self*, *Both*, *Other*, or *Bottle*. Data points show individual sessions (57 sessions). (**f**) Saccade reaction times (mean ± s.e.m., 57 sessions) for choosing *Self*, *Both*, *Other*, or *Bottle*. In the boxcar plots, blue lines represent the median; box edges represent the 25th and 75th percentiles; whiskers encompass all non-outlier data points; outliers are plotted as points in red.

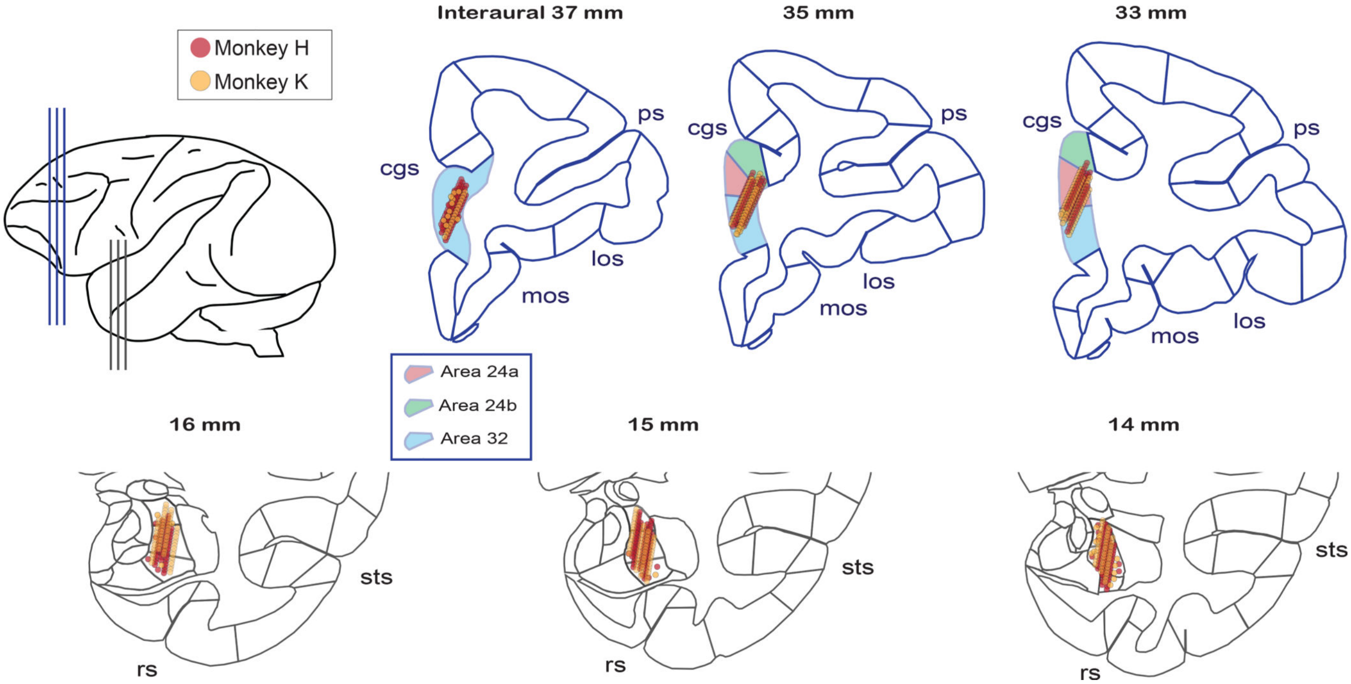

Fig. 2. Anatomical locations investigated for the coordination of spiking and LFP activity between BLA and ACCg.

Recording locations for individual cells and LFP sites from monkey H (red points) and monkey K (orange points) projected onto the standard stereotaxic coordinates of the rhesus macaque brain atlas[29]. For each area's projections, three representative coronal slices were chosen with a 2-mm interaural spacing for ACCg and with a 1-mm interaural spacing for BLA in the anterior-to-posterior dimension (as shown in the top left cartoon). Selected landmarks are labeled: cingulate sulcus (cgs), principle sulcus (ps), medial orbitofrontal sulcus (mos), lateral orbitofrontal sulcus (los), superior temporal sulcus (sts), and rhinal sulcus (rs). Boxed inset shows region assignments for the ACC Brodmann names based on the Paxinos atlas[29].

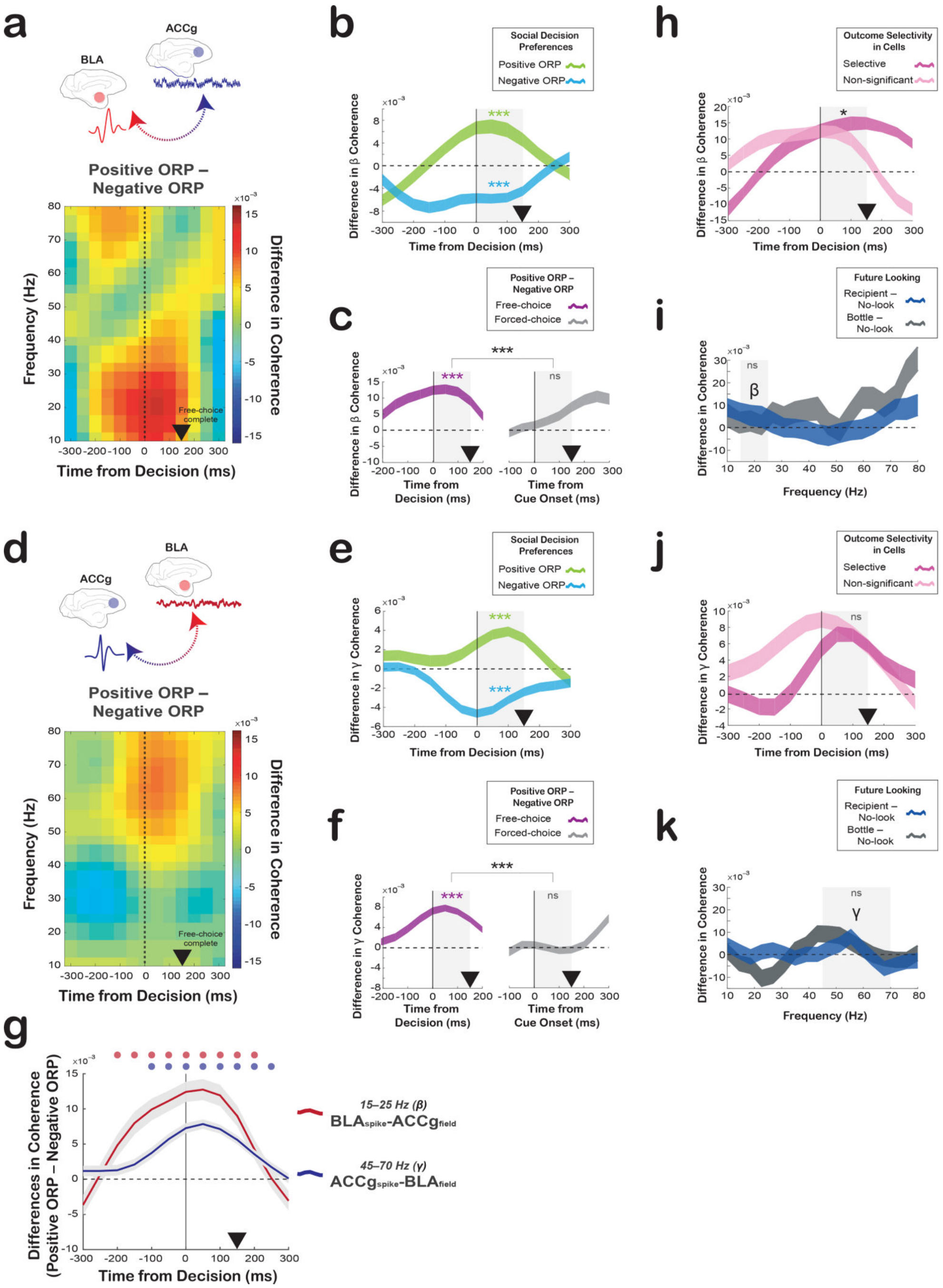

Fig. 3. Spike-field coherence between ACCg and BLA shows frequency-specific and free-choice-selective coordination for positive ORP compared to negative ORP.

(**a**) Differences in $\text{BLA}_{\text{spike}}$-$\text{ACCg}_{\text{field}}$ coherence values between expressing positive ORP (*Other–Bottle*) and negative ORP (*Self–Both*) over time and frequency aligned to the time of free-choice decision (n = 403 pairs). (**b**) Time courses of the spike-field coherence values in the beta frequency separately for positive ORP (light green; *Other–Bottle*) and negative ORP (light blue: *Self–Both*) (403 pairs). (**c**) Time courses of the beta spike-field coherence differences between expressing positive ORP and negative ORP on free-choice trials (purple; 403 pairs) and between the forced-choice construct of positive ORP (*Other-forced–Bottle-forced*) and the forced choice construct of negative ORP (*Self-forced–Both-forced*) on forced-choice trials (grey; 287 pairs). (**d**) Difference in $\mathrm{ACCg_{spike}}$-$\mathrm{BLA_{field}}$ coherence values between expressing positive ORP and negative ORP over time and frequency (1147 pairs). Same format as in a. (**e**) Time courses of the spike-field coherence values in the gamma frequency separately for positive ORP (light green) and negative ORP (light blue) (1147 pairs). (**f**) Time courses of the gamma spike-field coherence differences between positive and negative ORPs on free-choice (purple; 1147 pairs) trials and between the forced-choice construct of positive ORP and the forced-choice construct of negative ORP on forced-choice trials (grey; 956 pairs). (**g**) Average time courses of the beta band $\mathrm{BLA_{spike}}$-$\mathrm{ACCg_{field}}$ coherence (red; 403 pairs) and the gamma band $\mathrm{ACCg_{spike}}$-$\mathrm{BLA_{field}}$ coherence (blue; 1147 pairs) differences between the two ORPs (mean ± s.e.m.). Circles above the lines (in matching colors) show significant differences from zero ($p < 0.05$, Wilcoxon sign rank, two-sided; the individual p-values can be found in Supplementary Table 1). (**h**) Time courses of the spike-field coherence differences between the two ORPs on free-choice trials in the beta frequency separately for outcome selective (dark pink; 171 pairs) and non-significant cells (light pink; 232 pairs). (**i**) Differences in the $\mathrm{BLA_{spike}}$-$\mathrm{ACCg_{field}}$ coherence values over frequency between when the monkeys ultimately looked (compared to not looked) at the conspecific's face during the inter-trial interval (blue; looking at the conspecific minus no-looking) and when they ultimately looked (compared to not looked) at a bottle (gray; future looking at the bottle minus no-looking), collapsed over all outcomes (403 pairs). (**j**) Time courses of the gamma band spike-field coherence differences separately for outcome selective (dark pink; 548 pairs) and non-significant cells (light pink; 599 pairs) preferences. Same format as **h**. (**k**) Differences in the $\mathrm{ACCg_{spike}}$-$\mathrm{BLA_{field}}$ coherence values between looking at the conspecific's face and the bottle during the inter-trial interval (1147 pairs). Same format as **i**. In **b–c**, **e–f**, and **h–k**, significant coherence differences from zero (Wilcoxon sign rank, two-sided) are indicated by asterisks in matching colors and significant coherence differences between traces (Wilcoxon rank sum, two-sided) are indicated in black asterisks for the analyzed epoch (gray shading; 0–150 ms) (***, $p < 0.0001$; **, $p < 0.001$; *, $p = 0.02$; ns, not significant [panel **c**, $p = 0.17$; **i**, $p = 0.98$; **j**, $p = 0.11$; **f**, $p = 0.62$; **k**, $p = 0.94$]). In **b–c**, **e–f**, and **h–k**, the shaded traces represent ± s.e.m. centered around the mean. In all plots, the black arrowheads mark the time at which the monkeys completed a free-choice or forced-choice decision by maintaining gaze fixation on a chosen target or cue.

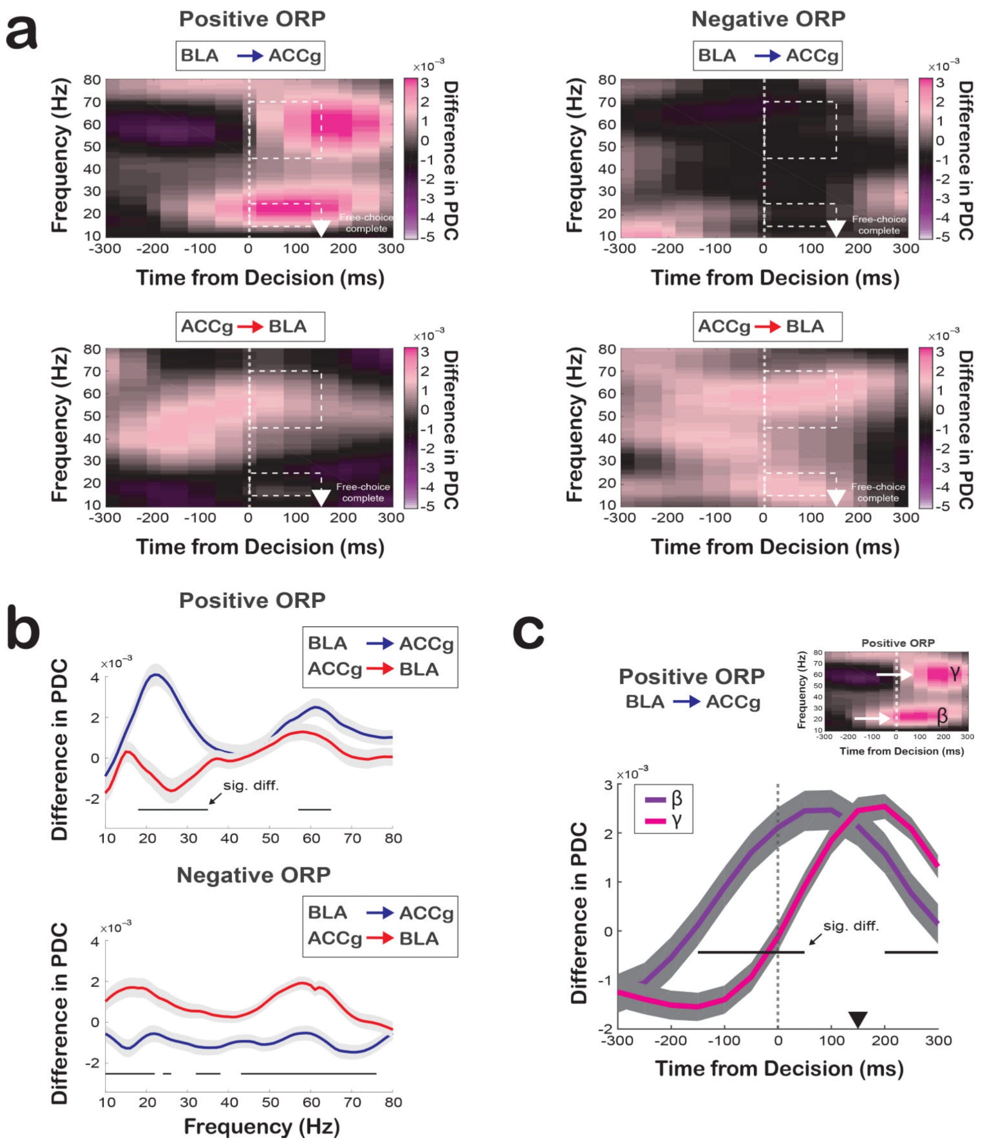

Fig. 4. Directionality of information flow between ACCg and BLA for positive ORP and negative ORP as a function of time and frequency.

(**a**) Frequency-domain directional influences assessed by partial directed coherence (PDC) on free-choice trials (n = 593 pairs). PDC values as a function of time and frequency for positive ORP (*Other*–*Bottle*) for BLA→ACCg (top left) and ACCg→BLA (bottom left), and PDC values for negative ORP (*Self*–*Both*) for BLA→ACCg (top right) and ACCg→BLA (bottom right). The white arrowheads mark the time at which the monkeys completed a free choice by maintaining fixation on a chosen target for 150 ms. Dotted lines indicate the beta (15–25Hz) and gamma (45–70Hz) band during the post-decision epoch. (**b**) Quantification of the directionality of information flow during the free-choice decision epoch as a function of frequency for positive ORP decision (top) and negative ORP (bottom) for BLA→ACCg (in blue) and ACCg→BLA (in red). Horizontal lines indicate significant differences between these PDC values ($p < 0.05$, Wilcoxon sign rank, two-sided; 593 pairs; individual p-values can be found in Supplementary Table 1). (**c**) Time courses of the beta and gamma band PDC differences for BLA→ACCg for positive ORP. In **b** and **c**, Horizontal lines indicate significant differences between these PDC values ($p < 0.05$, Wilcoxon sign rank, two-sided; 593 pairs; individual p-values can be found in Supplementary Table 1). Shaded regions represent standard errors.

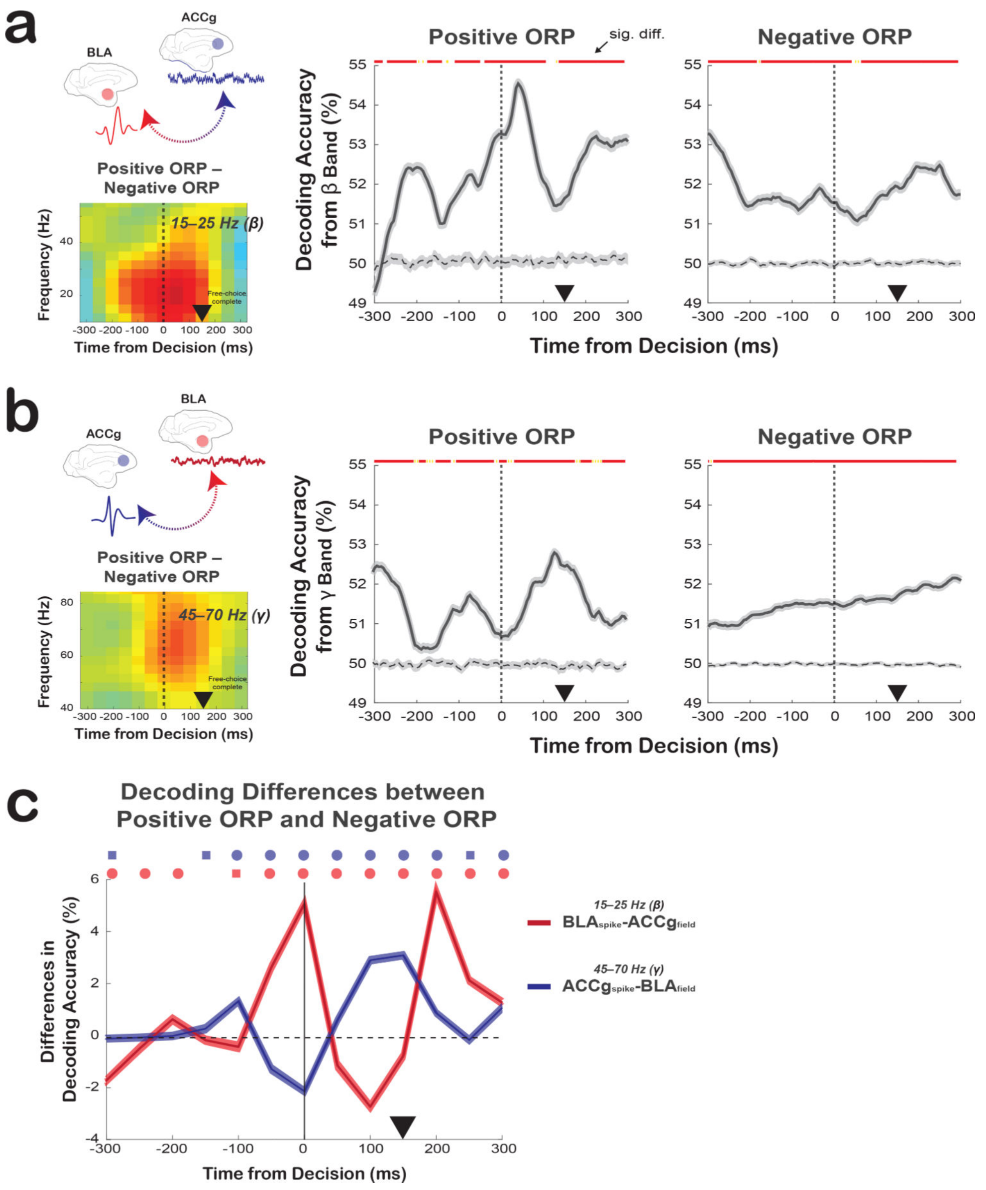

Fig. 5. Decoding social decisions directly from the spike-field relations between ACCg and BLA.

(**a**) Decoding performance using the $\mathrm{BLA}_{\mathrm{spike}}$-$\mathrm{ACCg}_{\mathrm{field}}$ coherence differences in the beta band (shown in the left inset; 403 pairs) for discriminating *Other* from *Bottle* (middle) and discriminating *Self* from *Both* (right) decisions over time (mean ± s.e.m.). Lines represent means of 100 permutation iterations with the shaded area representing s.e.m.. Dashed lines represent empirically determined null distribution. (**b**) Average decoding performance using the $\mathrm{ACCg}_{\mathrm{spike}}$-$\mathrm{BLA}_{\mathrm{field}}$ coherence in the gamma band (shown in the left inset; 1147 pairs) for discriminating *Other* from *Bottle* (middle) and discriminating *Self* from *Both* (right) decisions over time (mean ± s.e.m.). Lines represent means of 100 permutation iterations with the shaded area representing s.e.m.. Same format as in **a**. In **a** and **b**, lines at the top indicate significant differences from the null in each of the 5 ms bin (red: $p < 0.0001$, yellow: $p < 0.05$, Wilcoxon sign rank, two-sided; individual p-values can be found in Supplementary Table 1). (**c**) Differences in decoding performances between *Other*/*Bottle* and *Self*/*Both* contexts from the beta BLA_{spike}-$ACCg_{field}$ coherence (red; 403 pairs) and the gamma $ACCg_{spike}$-BLA_{field} coherence (blue; 1147 pairs). Lines represent mean differences from 100 permutation test iterations with the shaded area representing s.e.m.. Symbols above the lines (in matching colors) show significant differences from zero (circle: $p < 0.0001$, square, $p < 0.05$, Wilcoxon sign rank, two-sided; individual p-values can be found in Supplementary Table 1). In all plots, the black arrowheads mark the time at which the monkeys completed a free-choice decision by maintaining fixation on a chosen target for 150 ms.